Quantification of local changes in myocardial motion by diffeomorphic registration via currents: Application to paced hypertrophic obstructive cardiomyopathy in 2D echocardiographic sequences

Nicolas Duchateau, Geneviève Giraldeau, Luigi Gabrielli, Juan Fernández-Armenta, Diego Penela, Reinder Evertz, Lluis Mont, Josep Brugada, Antonio Berruezo, Marta Sitges, et al.

To cite this version:

Nicolas Duchateau, Geneviève Giraldeau, Luigi Gabrielli, Juan Fernández-Armenta, Diego Penela, et al.. Quantification of local changes in myocardial motion by diffeomorphic registration via currents: Application to paced hypertrophic obstructive cardiomyopathy in 2D echocardiographic sequences. Medical Image Analysis, 2015, 19 (1), pp.203-219. 10.1016/j.media.2014.10.005 . hal-02282407

HAL Id: hal-02282407
https://hal.science/hal-02282407v1

Submitted on 11 Sep 2019

Quantification of local changes in myocardial motion by diffeomorphic registration via currents:

Application to paced hypertrophic obstructive cardiomyopathy in 2D echocardiographic sequences

Nicolas Duchateau[a,b,*], Geneviève Giraldeau[a,c], Luigi Gabrielli[a,d], Juan Fernàndez-Armenta[a], Diego Penela[a], Reinder Evertz[a], Lluis Mont[a], Josep Brugada[a], Antonio Berruezo[a], Marta Sitges[a], Bart H Bijnens[b,e]

[a] *Hospital Clínic - IDIBAPS - Universitat de Barcelona, Spain*
[b] *Universitat Pompeu Fabra, Barcelona, Spain*
[c] *Université de Montréal, Montreal Heart Institute, Canada*
[d] *Advanced center for chronic diseases. Escuela de medicina. Pontificia Universidad Católica, Santiago, Chile*
[e] *ICREA, Barcelona, Spain*

Abstract

Time-to-peak measurements and single-parameter observations are cumbersome and often confusing for quantifying local changes in myocardial function. Recent spatiotemporal normalization techniques can provide a global picture of myocardial motion and strain patterns and overcome some of these limitations. Despite these advances, the quantification of pattern changes remains descriptive, which limits their relevance for longitudinal studies. Our paper provides a new perspective to the longitudinal analysis of myocardial motion. Non-rigid registration (diffeomorphic registration via currents) is used to match pairs of patterns, and pattern changes are inferred from the registration output. Scalability is added to the different components of the input patterns in order to tune up the contributions of the spatial, temporal and magnitude dimensions to data changes, which are of interest for our application. The technique is illustrated on 2D echocardiographic sequences from 15 patients with hypertrophic obstructive cardiomyopathy. These patients underwent biventricular pacing, which aims at provoking mechanical dyssynchrony to reduce left ventricular outflow tract (LVOT) obstruction. We demonstrate that our method can automatically quantify timing and magnitude changes in myocardial motion between baseline (non-paced) and 1 year follow-up (pacing on), resulting in a more robust analysis of complex patterns and subtle changes. Our method helps confirming that the reduction of LVOT pressure gradient actually comes from the induction of the type of dyssynchrony that was expected.

Keywords: Diffeomorphic registration, currents, deformation-based morphometry, speckle-tracking, myocardial motion, hypertrophic cardiomyopathy.

---

1. Introduction

1.1. Comparison of myocardial motion patterns

1.1.1. General context and methods

The study of cardiac function in current clinical practice and research relies on the extraction of pathophysiologically-relevant features from image sequences. Dynamic markers of common use consist of myocardial displacement, velocity, strain and strain rate (Bijnens et al., 2009, 2012). Their estimation results from the propagation of cardiac wall segmentations along the cycle. This is achieved by means of 2D/3D+t segmentation techniques or non-rigid registration along image sequences (Tobon-Gomez et al., 2013; De Craene et al., 2013), or speckle-tracking, which predominates in echocardiography (Duchateau et al., 2013a; Jasaityte et al., 2013). An extensive clinical review is given in Cikes et al. (2010) in the concrete case of our application:

---

[*] corresponding author.
Address: DTIC, Universitat Pompeu Fabra (office 55.107), c/ Tànger 122-140, E08018 Barcelona, Spain.
Tel: +34 93-542-1348. Email: `nicolas.duchateau@upf.edu`

hypertrophic cardiomyopathies.

However, the complexity of the myocardial motion/strain patterns, and inter-subject differences in size and timing of the heart limit the use of such techniques (Fornwalt, 2011). Studies focus on individual qualitative descriptions or on single quantitative indices describing part of the patterns (time-to-event and regional/local single values, mainly).

In contrast, we believe that quantitative comparison of patterns is possible at a more comprehensive level by the use of computational anatomy techniques (Miller and Qiu, 2009). This requires to normalize the studied data to a reference system of spatiotemporal coordinates, as settled in statistical atlas applications (Duchateau et al., 2011). *Anatomical normalization* generally builds upon parallel transport techniques (Qiu et al., 2009; Duchateau et al., 2012a; Lorenzi and Pennec, 2013). *Temporal normalization* addresses possible variations in the length of the cardiac cycle and its intrinsic physiological phases (Perperidis et al., 2005; Duchateau et al., 2011; Russell et al., 2012). In the present paper, we build upon these concepts for normalizing the data prior to any quantitative comparison (baseline and follow-up data, and inter-subject comparisons).

1.1.2. *Voxel-based vs. pattern-based comparisons*

Despite these advances, the pattern analysis is still descriptive and often performed through a voxel-based representation. On the contrary, the purpose of our application (quantifying pattern changes in longitudinal studies) requires relevant *pattern-wise representations*. Attempts towards such representations mainly take into account inter-voxel dependences. They consist of global techniques for dimensionality reduction (Ashburner and Klöppel, 2011), as also applied to myocardial motion (McLeod et al., 2013), or eventually multiscale decomposition techniques (Lorenzi et al., 2013; Bhatia et al., 2014). Neighborhood graphs have been used to represent disease evolution on a population of cardiac motion patterns (Duchateau et al., 2012c), and may serve for the study of changes under the effect of time and treatment (Duchateau et al., 2013b).

Nonetheless, none of these techniques is explicitly designed for the estimation of changes between patterns, which is our primary interest here.

1.1.3. *Methods specific to the recovery of changes*

A first branch of methods builds upon Dynamic Time Warping (DTW) (Sakoe and Chiba, 1978). This consists in computing a correspondence matrix between the data to match, and estimating a warping of the data from the optimal path along this matrix. Variants include improved metrics (Sakoe and Chiba, 2009), refined construction of this path (Nielsen et al., 1998), and eventually the estimation of smoother warps (Zhou and De la Torre, 2012). However, these methods present several fundamental drawbacks for our application: (i) as warping techniques, their robustness towards very different shape evolution behaviors (as encountered in our data, Sec.3.2.2) may be limited; (ii) they assume that all parts of the anatomy evolve at the same speed along the cardiac cycle, which is not the case in our application. Neighboring locations along the myocardium may have a close behavior but evolve differently; (iii) finally, they are based on landmark correspondences, while more robust features such as measures or currents have been proposed to overcome the limits of landmark matching (Glaunès, 2005).

We prefer to build upon the principles of *deformation-based morphometry* (Ashburner and Friston, 2003; Ashburner et al., 1998). This consists in analyzing the warping necessary to match different data, coming either from different subjects or from the longitudinal study of a single subject. We apply this strategy to the matching of functional data (myocardial motion), which we manage as smooth spatiotemporal shapes (Sec.2.1.1 and 2.2). We preferred a generic surface matching approach that is diffeomorphic (Trouvé, 1998) to prevent any folding in the data correspondence. Indeed, by nature, the cardiac anatomy cannot fold. The functional data patterns attached to it may change under the therapy, but such functional data still should be warped in a way compliant with the anatomy, and therefore diffeomorphic.

The registration scheme uses currents (Glaunès, 2005; Vaillant and Glaunès, 2005; Durrleman et al., 2009, 2011). In this way, surfaces are compared without the need for point-to-point correspondences. Additionally, this makes the registration robust to changes in parametrization and physiological behavior (concavity/convexity mainly, which are very likely to happen in our application).

1.1.4. Towards a generic transformation model?

Other registration-based approaches for the matching of dynamic series are extensively discussed in Durrleman et al. (2013) for atlas building purposes. The relevance of this work is two-fold for our application. First, it builds upon shape warping and fitting via continuous diffeomorphic transformations from the large deformation diffeomorphic metric mapping (LDDMM) framework (Beg et al., 2005; Miller et al., 2002). This aspect is shared by the registration via currents that we use (Glaunès, 2005). Then, it settles the foundations of a generic framework for the statistical analysis of dynamic shape evolutions. The objectives of our study (comparison of individual shape evolutions between baseline and follow-up) present similarities with the comparison of growth scenarios targeted in Durrleman et al. (2013)

For the comparison of growth scenarios, the authors recommend a subject-specific approach. This leads to a transform model that separates the problem into the recovery of a purely spatial transform $\Phi_{space}(\mathbf{x})$ and a purely temporal one $\Phi_{time}(t)$, namely: $\Phi(\mathbf{x}, t) = (\Phi_{space}(\mathbf{x}), \Phi_{time}(t))$. This model seems adequate for longitudinal studies in neuroimaging or evolution scenarios, where one can assume that $\Phi_{time}(\mathbf{x}, t) \approx \Phi_{time}(t)$, namely that different parts of the anatomy evolve at the same speed (e.g. age or time along the longitudinal study). The spatial transform is assumed independent from time, namely: $\Phi_{space}(\mathbf{x}, t) \approx \Phi_{space}(\mathbf{x})$. Such hypotheses are not valid for our application: for the study of changes along cardiac sequences, different parts of the anatomy may clearly evolve at different speeds (e.g. the septal and lateral walls). Thus, we think that considering spatial and timing changes together, with the most general form of transformations $\Phi(\mathbf{x}, t)$ can be more relevant to our application.

Nonetheless, this model has higher complexity, and cannot be directly used as such for a statistical analysis. Thus, we introduce a-priori to our model through scaling factors on each dimension of the input data. This serves for conditioning the problem to solutions relevant for our application, as detailed further in the Methods section.

1.2. Hypertrophic obstructive cardiomyopathy

Hypertrophic cardiomyopathy (Gersh et al., 2011) is a genetic disease that alters the cellular contractility of the cardiac muscle, leading to myocyte hypertrophy and larger wall thickness of the myocardium, typically at the left ventricle. Altered contractility first implies a decrease in the local myocardial contraction, and is accompanied by changes in the myocardial geometry (hypertrophy of affected segments). The hypertrophic septum may provoke in some patients a severe obstruction of the left ventricular outflow tract (LVOT). This may severely alter the cardiac pump performance, increase LV pressure and wall stress, and the risk of sudden death due to myocardial fibrosis and arrhythmia induction (Maron et al., 2003).

Biventricular pacing has been suggested as a potential alternative to surgery to reduce the obstruction (Berruezo et al., 2011; Vatasescu et al., 2012). This is the treatment received by the patients of our study. The aim of this process is to provoke a controlled mechanical dyssynchrony in the ventricles, so that the local geometry at the LVOT is changed, and the temporal window for the blood to go out of the LV is enlarged. The procedure is optimized to reach the best maximum decrease in LVOT obstruction time and pressure gradient. The benefits of this intervention predominate over potential deteriorations of the cardiac function as consequence of the induced dyssynchrony (Giraldeau et al., 2013).

Observations of clinicians are mainly visual, due to the lack of an adequate technique for pattern comparison. This procedure would therefore highly benefit from efficient monitoring of the changes in cardiac function induced by pacing. The technical difficulty of such a setting is to be able to recognize and measure these (possibly subtle) changes. The underlying objective is not to discriminate between responders and non-responders, which is already known by measuring LVOT pressure gradient, but to assess that gradient reduction actually comes from the induction of the type of dyssynchrony that was expected.

1.3. Proposed approach

Based on this, we propose to estimate myocardial motion pattern changes by diffeomorphic non-rigid registration. Myocardial motion data are considered as 3D shapes, and are registered using currents (Glaunès, 2005; Vaillant and Glaunès, 2005; Durrleman et al., 2009, 2011). Pattern changes are inferred from the matching of baseline and follow-up data and compared among the whole population. To the best of our knowledge, this approach is new and constitutes the main originality of our work. A second contribution of the present paper is in the adaptation of the data so that the contributions of

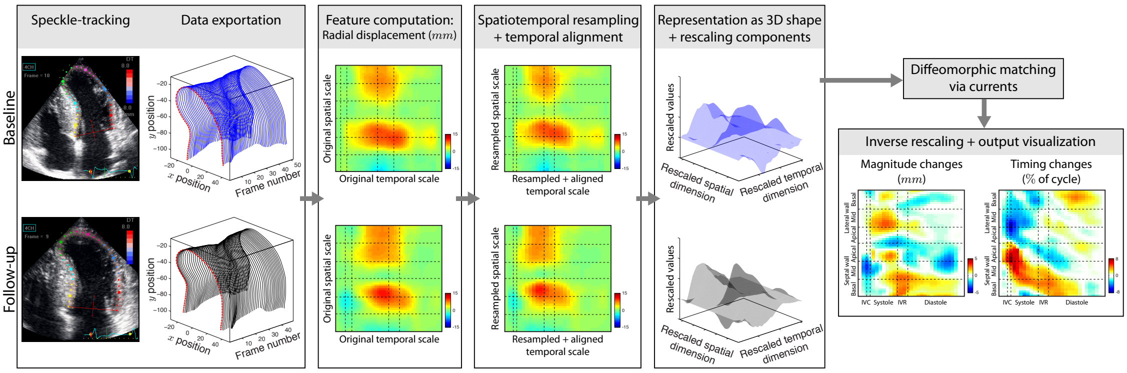

Figure 1: Pipeline for the method presented in this paper.

the spatial, temporal and magnitude dimensions are tuned up in the registration framework, as aimed at by the clinical context of our application.

The clinical potential of the method is illustrated on a dataset of 15 HOCM patients undergoing biventricular pacing to induce dyssynchrony and reduce the LVOT obstruction. Pattern changes may be complex and sometimes subtle. We demonstrate that our method allows the assessment of these changes, and discuss the relevance of the estimated values with respect to clinical expectations.

2. Methods

The processing pipeline used in this paper is illustrated in Fig.1 and algorithm 1, and described in the following sections.

Algorithm 1: Overall pipeline.

```
for subject $k$ do
    for sequence $s \in \{OFF, FU\}$ do
        Export position of myocardial centerline
            $\mathbf{X}(\mathbf{x_i}, t_j) \quad \forall i \in [1, N_\mathbf{x}],\ \forall j \in [1, N_t]$ ;
        Compute radial displacement
            $\varphi_r(\mathbf{x_i}, t_j) = \langle \mathbf{X}(\mathbf{x_i}, t_j) - \mathbf{x}_i, \mathbf{e}_r(\mathbf{x_i}, t_j) \rangle$ ;
                /* $\mathbf{e}_r$: radial direction */
        Resample data
            $\varphi_r(\mathbf{x_i}, t_j) \quad \forall i \in [1, N_\mathbf{x}^{REF}],\ \forall j \in [1, N_t^{REF}]$ ;
    Set $\alpha = 100,\ \lambda = 1,\ \beta = \beta_{balanced}$ ;
    for sequence $s \in \{OFF, FU\}$ do
        Rescale data
            $\hat{\varphi}_r(\mathbf{x}_i, t_j) = \lambda\, \varphi_r(\alpha\, \mathbf{x}_i, \beta\, t_j)$ ;
        Create 3D shape
            $S = \sum_f \delta_{\mathbf{c}_f}^{\mathbf{n}_f}$
            $f = [\hat{\varphi}_r(\mathbf{x}_i, t_j); \hat{\varphi}_r(\mathbf{x}_i, t_{j+1}); \hat{\varphi}_r(\mathbf{x}_{i+1}, t_{j+1})]$
           or $[\hat{\varphi}_r(\mathbf{x}_{i+1}, t_j); \hat{\varphi}_r(\mathbf{x}_i, t_{j+1}); \hat{\varphi}_r(\mathbf{x}_{i+1}, t_{j+1})]$ ;
    Register $\hat{\varphi}_r^{FU} \overset{\phi}{\mapsto} \hat{\varphi}_r^{OFF}$;
    Rescaling by $1/\lambda$, $1/\alpha$ and $1/\beta$;
```

2.1. Motion extraction

2.1.1. Speckle-tracking and data exportation

The myocardium is tracked along the cardiac cycle using commercial 2D speckle-tracking (Echopac v110.1.2, GE Healthcare, Milwaukee, WI) on 4-chamber echocardiographic sequences. The speckle-tracking algorithm and other registration-based algorithms share similar concepts (Tobon-Gomez et al., 2013; De Craene et al., 2013; Duchateau et al., 2013a; Jasaityte et al., 2013). Although the manufacturer gives few details about its implementation, we believe that the algorithm is based on the principles given in Adam et al. (2004); Behar et al. (2004); Leitman et al. (2004). We decided to use it in our application due to its computational speed (around 2-3s per cardiac sequence), its wide use in the clinical community, and its practical interface for manual re-adjustments of the initial segmentation. The repeatability of the tracking procedure is discussed in App.A. The tracking performance is illustrated in Fig.2 on the baseline and follow-up echocardiographic sequences of a HOCM patient. An animated version of this figure is available as *Online Supplement*.

In our protocol[1], the endocardium is manually segmented at end-systole using the control-point delineation proposed by the software interface, before its propagation along the cycle. Drift removal is used to achieve cyclic motion. No additional spatial/temporal smoothing is added.

---

[1] The implementation of the speckle-tracking data post-processing and spatiotemporal normalization was realized using Matlab v.R2011a (MathWorks, Natick, MA), and is publicly available online at: `http://nicolasduchateau.wordpress.com/downloads/`

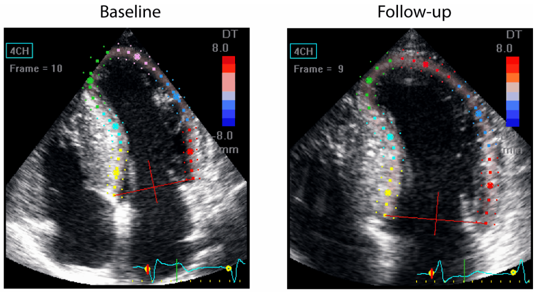

Figure 2: Speckle-tracking on the baseline and follow-up echocardiographic sequences of a HOCM patient (animated version as *Online Supplement*).

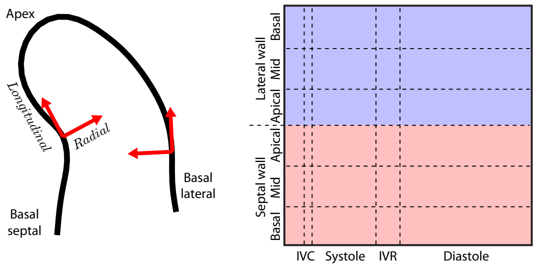

Figure 3: Left: myocardial centerline and associated local directions. Right: representation used to visualize 2D + t data. IVC/IVR: isovolumetric contraction/relaxation.

This leads to the exportation of the position of the myocardial centerline along the cycle $\mathbf{X}(\mathbf{x_i}, t_j)$, where $\{\mathbf{x_i}, t_j\}_{j\in[1,N_t]}^{i\in[1,N_\mathbf{x}]}$ is its spatiotemporal discrete parameterization, $N_\mathbf{x}$ is the number of landmarks defining the myocardial centerline and N_t is the number of frames in the considered cycle. Note that $\mathbf{X}(\mathbf{x_i}, 0) = \mathbf{x_i}$, and that $N_\mathbf{x}$ and N_t are specific to the subject and sequence studied.

2.1.2. *Computation of the features of interest*

Myocardial displacement, velocities, strain and strain rate can easily be computed from the myocardial centerline data. We decided to center our study on the radial component of the displacement, which is more relevant for our application. Indeed, the LV obstruction occurs at the outflow tract, which connects to the aorta, and is due to an hypertrophic septum. Thus, theoretically, the higher the dyssynchrony on radial displacement, the larger the interval through which the flow can go out of the LV. This observation is not so intuitive from the longitudinal component of displacement (different patterns) and strain (almost no strain along the septum due to hypertrophy). It should be noted that our framework is generic and could be straightforwardly applied to any component of myocardial functional data, and not only to radial displacement. Additionally, our observations could be refined by the incorporation of multivariate data (e.g. the different components of displacement, or displacement and strain together). However, this would require the non-trivial adaptation of the registration framework of Sec.2.2 to this type of data.

Displacement vectors are computed from the position of the myocardial centerline using $\varphi(\mathbf{x_i}, t_j) = \mathbf{X}(\mathbf{x_i}, t_j) - \mathbf{x_i}$. Radial displacement corresponds to their projection along the radial direction of the myocardium $\varphi_r(\mathbf{x_i}, t_j) = \langle \mathbf{X}(\mathbf{x_i}, t_j) - \mathbf{x}_i, \mathbf{e}_r(\mathbf{x_i}, t_j)\rangle$.

For descriptive visualization purposes, a convenient way of observing this 2D + t data consists of color-coded maps inspired from anatomical M-mode echocardiography (Fig.3). Time (the cardiac cycle) is used as horizontal axis, while the spatial position along the myocardium is used as vertical axis. A real data example of this representation is given in Fig.4 (baseline and follow-up data).

2.1.3. *Spatiotemporal resampling and normalization*

The data from the speckle-tracking does not immediately allow statistical comparisons. Each sequence differs from the others in terms of anatomy, relative timing of physiological events, and duration of the cardiac cycle. For this, we use a spatiotemporal normalization scheme that redefines data in a common system of coordinates. With such a normalization, our method only recovers actual pattern changes and is not biased by the above-listed physiological differences. Our framework builds upon Duchateau et al. (2011), but the present implementation is more closely adapted from the one in Duchateau et al. (2012a)[1].

One main difference should be noted with respect to these schemes. In the present paper, a segmentation of the myocardial wall is provided by the speckle-tracking procedure. This implies that local anatomical coordinates (radial and longitudinal directions, in our case) are already known for each subject. Additionally, if the data of each subject are resampled to a common sampling (as done in the present framework), correspondence between anatomical locations along the myocardium can be assumed. Thus, there is equivalence between the two following processes, considering the displacement vector of a given subject at a given spatiotem-

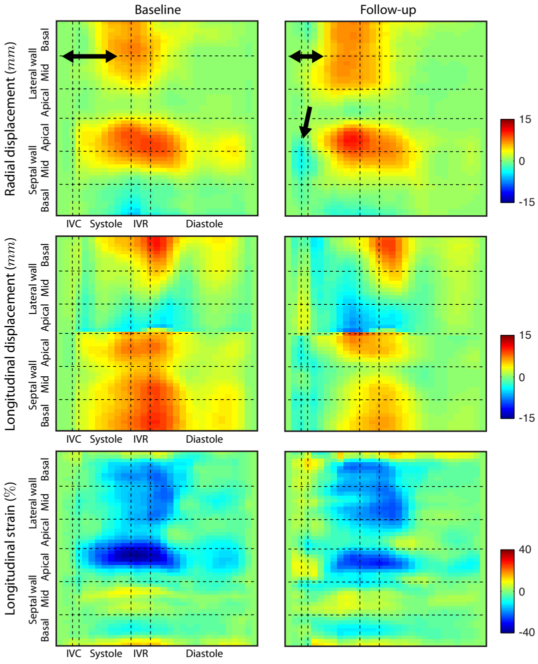

Figure 4: Myocardial displacement and strain maps at baseline and follow-up for the patient shown in Fig.2. Black arrows point out noticeable changes induced by pacing: earlier activation of the lateral wall and early-systole outward motion of the septum. These changes are mainly visible on radial displacement (top), while longitudinal displacement (middle) and longitudinal strain (bottom) are less relevant for our specific clinical application.

poral location: (i) looking at its radial/longitudinal components at this location or at its corresponding location in the reference anatomy; and (ii) rotating it, from the radial/longitudinal system of coordinates at this location to the radial/longitudinal system of coordinates of the reference anatomy at this anatomical location, and looking at its radial/longitudinal components. Given this, our implementation is equivalent to the rotation-only scheme in a Lagrangian point-of-view described in Duchateau et al. (2012a).

The issue of including a scaling factor in the spatial normalization between subjects is still an open question (Duchateau et al., 2012a). It was not considered in our implementation, which only features a spatiotemporal resampling step and a temporal normalization step. No average anatomy computation and no additional spatial normalization are considered.

Data normalization therefore consists of the following steps:

a. Resampling. Data is resampled to a common parametrization[2] prior to the spatiotemporal normalization steps. Cubic splines are used to obtain an approximation of the data on a continuous timescale and along the whole myocardial centerline. For the sake of simplicity and computational speed, we preferred this scheme against more advanced ones, such as diffeomorphic-compliant spline interpolation (Trouvé and Vialard, 2012; Vialard and Trouvé, 2010).

b. Temporal normalization. Sequences dynamics are matched based on piece-wise linear warping of the timescale, so that representative physiological events are matched. Our implementation uses the onset of QRS (identified on the electrocardiogram), and mitral/aortic valves opening and closure, identified using continuous-wave Doppler imaging on the corresponding valve or visual assessment from B-mode images).

Note that these pre-alignment transforms are diffeomorphic by nature. Also, they contain information reflecting part of the inter- and intra-subject variability (Sec.3.3.2). However, contrary to Durrleman et al. (2013) who include these "changes of coordinates" in their transform model, we are not interested in analyzing such correspondences but the remainder of these normalization steps. This coincides with a vast majority of morphometry approaches, e.g. in neuroimaging applications, where brain images are first aligned by rigid or affine transforms. Only the remaining differences, estimated by non-rigid registration, are analyzed and included in the statistical analysis.

After these steps, radial displacement data is referred to as $\varphi_r(\mathbf{x_i}, t_j)$, where $\{\mathbf{x_i}\}_{i\in[1,N_{\mathbf{x}}^{REF}]}$ now corresponds to the set of landmarks defining the myocardial centerline of the reference anatomy, and $\{t_j\}_{j\in[1,N_t^{REF}]}$ stands for the temporal instants of the reference cycle.

---

[2] The currents used in the registration of Sec.2.2 do not require the same parametrization for the data to be matched. Thus, the resampling step may be considered unnecessary. However, this resampling is useful for the spatiotemporal normalization steps of our pipeline, which would require in any case data interpolation.

2.1.4. Explicit shape representation

The 2D + t radial displacement data of a given subject and sequence are considered as a spatiotemporal 3D shape, where the three dimensions correspond to magnitude, spatial location and time along the cycle.

We use an explicit triangular shape representation as required by the registration algorithm. A face f is either formed by the triangles:

$$\begin{aligned} &[\ \varphi_r(\mathbf{x}_i, t_j)\ ;\ \varphi_r(\mathbf{x}_i, t_{j+1})\ ;\ \varphi_r(\mathbf{x}_{i+1}, t_{j+1})\ ] \\ &\text{or} \\ &[\ \varphi_r(\mathbf{x}_{i+1}, t_j)\ ;\ \varphi_r(\mathbf{x}_i, t_{j+1})\ ;\ \varphi_r(\mathbf{x}_{i+1}, t_{j+1})\ ]\,. \end{aligned} \tag{1}$$

Changes between baseline (φ_r^{OFF}, pacing-off) and follow-up (φ_r^{FU}) data now can be estimated by 3D surface matching, instead of trying to register 2D + t functional data. A more generic approach using 3D + t data or 2D + t vector fields should use a generalized formulation of the registration via currents, which may be challenging (Charon and Trouvé, 2014).

Note that such an explicit shape representation is not a problem for our application. Meshing errors and other limits specific to explicit shape representations are prevented by the registration via currents, which (i) does not require point-to-point correspondences, (ii) considers the shapes up to a certain level of geometric details conditioned by the smoothness of the vector fields on which currents operate (Sec.2.2.1), and (iii) allows multiresolution strategies to improve the matching performance.

2.2. Diffeomorphic registration via currents

2.2.1. Representation of shapes as currents

The speckle-tracking segmentation and the spatial resampling and normalization steps may let us assume spatial point-to-point correspondence (Sec.3.2.1). However, point-to-point correspondence in the timing of events cannot be assumed. Otherwise, the estimation of changes in the temporal component of our data could be achieved by a simpler and faster diffeomorphic landmark matching algorithm (Glaunès et al., 2004). For this reason, our implementation performs surface matching by diffeomorphic registration via currents, as proposed in Glaunès (2005).

We denote $\mathcal{W}$ a reproducible kernel Hilbert space (RKHS) (Aronszajn, 1950; Saitoh, 1988; Glaunès, 2005) of vector fields $\mathbb{R}^3 \to \mathbb{R}^3$. Its associated kernel is denoted $k_{\mathcal{W}} : \mathbb{R}^3 \times \mathbb{R}^3 \to \mathbb{M}_{3,3}$, where $\mathbb{M}_{3,3}$ is the set of 3×3-dimensional real-value matrices. The elements of $\mathcal{W}$ are vector fields resulting from the convolution between any square-integrable vector field and the kernel $k_{\mathcal{W}}$. In practice, we choose an isotropic Gaussian kernel of the form $k_{\mathcal{W}}(\mathbf{x}, \mathbf{y}) = \exp\left(\frac{-\|\mathbf{x}-\mathbf{y}\|^2}{\sigma_{\mathcal{W}}^2}\right)\mathbf{I}$, where $\mathbf{I}$ is the identity, so that the smoothness of the vector fields $\mathbf{w} \in \mathcal{W}$ is controlled by the bandwidth $\sigma_{\mathcal{W}}$.

A Dirac current $\delta_{\mathbf{c}}^{\mathbf{n}}$ applied to a given $\mathbf{w} \in \mathcal{W}$ can be seen as the realization of $\mathbf{w}$ with respect to the oriented segment $\mathbf{n}$ at point $\mathbf{c}$, defined as: $\delta_{\mathbf{c}}^{\mathbf{n}}(\mathbf{w}) = \langle \mathbf{w}(\mathbf{c}), \mathbf{n}\rangle_{\mathbb{R}^3} \in \mathbb{R}$. Thus, a triangulated surface can be characterized by a discrete current S defined as the finite sum of Dirac currents $S = \sum_f \delta_{\mathbf{c}_f}^{\mathbf{n}_f}$, where f is a triangular face of the considered surface, $\mathbf{c}_f$ its center, and $\mathbf{n}_f$ its normal vector.

The normal vector $\mathbf{n}_f$ corresponds to the cross-product of the vectors defining its two first edges, and therefore also encodes the area of the face f.

We denote $\mathcal{W}^*$ the dual space of $\mathcal{W}$, which is equipped with the inner product $\langle .,. \rangle_{\mathcal{W}^*}$ (Glaunès, 2005; Vaillant and Glaunès, 2005). From the above definition, Dirac currents belong to $\mathcal{W}^*$, and the inner product between two Dirac currents is $\langle \delta_{\mathbf{c_1}}^{\mathbf{n_1}}, \delta_{\mathbf{c_2}}^{\mathbf{n_2}} \rangle_{\mathcal{W}^*} = {}^t\mathbf{n_1}\ k^{\mathcal{W}}(\mathbf{c_1}, \mathbf{c_2})\ \mathbf{n_2}$, where ^{t} is the transpose operator.

Finally, the dual norm of a discrete current $S = \sum_f \delta_{\mathbf{c}_f}^{\mathbf{n}_f}$ is given by:

$$\|S\|^2_{\mathcal{W}^*} = \sum_{f,f'} {}^t\mathbf{n_f}\ k^{\mathcal{W}}(\mathbf{c_f}, \mathbf{c_{f'}})\ \mathbf{n_{f'}}. \tag{2}$$

2.2.2. General registration framework

The above-described formulation can be used to define the similarity metric for a registration problem (Glaunès, 2005; Vaillant and Glaunès, 2005).

We denote φ_r^{OFF} and φ_r^{FU} the two triangulated surfaces to register, and S^{OFF} and S^{FU} their associated discrete currents. The registration problem will look for a diffeomorphic matching ϕ between φ_r^{OFF} and φ_r^{FU}, such that the transported current $\phi_\sharp S^{FU}$ and the target one S^{OFF} match as best as possible ($\phi_\sharp$ is the push-forward of ϕ on the current associated to S). Thus, in terms of global energy for our registration problem, the *similarity metric* can be set as:

$$\|\phi_\sharp S^{FU} - S^{OFF}\|^2_{\mathcal{W}^*} \tag{3}$$

The diffeomorphic matching ϕ is constructed as the flow of a smooth velocity field $\mathbf{v}_\tau$, integrated by varying τ from 0 to 1, namely:

$$\frac{\partial \phi_\tau(\mathbf{x})}{\partial \tau} = \mathbf{v}_\tau(\phi_\tau(\mathbf{x})), \quad (4)$$
$$\text{with } \phi_0(\mathbf{x}) = \mathbf{x} \text{ and } \phi_1(\mathbf{x}) = \phi(\mathbf{x}).$$

The smoothness of $\mathbf{v}_\tau$ means that $\forall \tau \in [0,1]$, $\mathbf{v}_\tau$ belongs to a RKHS $\mathcal{V}$ with kernel $k_\mathcal{V}(\mathbf{x},\mathbf{y}) = \exp\left(\frac{-\|\mathbf{x}-\mathbf{y}\|^2}{\sigma_\mathcal{V}^2}\right)\mathbf{I}$, where $\sigma_\mathcal{V}$ controls the smoothness of $\mathbf{v}_\tau$. Thus, the *regularity* of the diffeomorphism is measured by:

$$\int_0^1 \|\mathbf{v}_\tau\|_\mathcal{V}^2 \mathrm{d}\tau. \quad (5)$$

In summary, the diffeomorphic matching ϕ between the two surfaces φ_r^{OFF} and φ_r^{FU} corresponds to the minimization of:

$$E(\phi) = \|\phi_\sharp S^{FU} - S^{OFF}\|_{\mathcal{W}^*}^2 + \gamma \int_0^1 \|\mathbf{v}_\tau\|_\mathcal{V}^2 \mathrm{d}\tau, \quad (6)$$

where γ is a scalar weight between the similarity and regularization terms.

In practice, we used the implementation of Glaunès (2005); Vaillant and Glaunès (2005), which is publicly available at `http://www.mi.parisdescartes.fr/~glaunes/matchine.zip`. Insights about the choice of the parameters $\sigma_\mathcal{W}$, $\sigma_\mathcal{V}$ and γ are given in Sec.3.2.2.

2.3. Tuning up spatial, temporal and magnitude contributions

In order to tune up the contributions of the spatial, temporal and magnitude dimensions of our data, we create a rescaled version of the displacement data φ_r:

$$\hat{\varphi}_r(\mathbf{x}_i, t_j) = \lambda\, \varphi_r(\alpha\, \mathbf{x}_i, \beta\, t_j), \quad (7)$$

where α, β and λ are scaling factors over the spatial, temporal and magnitude components of the displacement data, respectively.

These rescaled data serve as input for the registration scheme introduced in Sec.2.2.2. Finally, the spatial, temporal and magnitude variations are obtained at the original scale of our data by rescaling the components of the mapping ϕ by the inverse of the scaling factors, namely $1/\lambda$, $1/\alpha$ and $1/\beta$. The order in which these steps are included in our pipeline is summarized in algorithm 1.

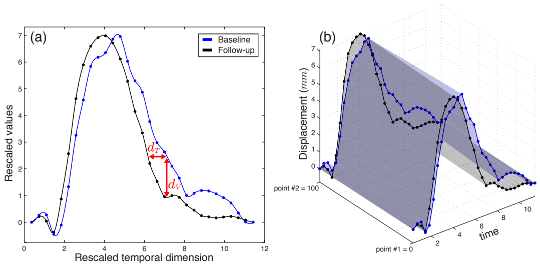

Figure 5: (a) Distances d_V and d_T used to tune the rescaling factors β and λ. (b) Two-locations signals used to understand the influence of the method parameters (scaling factors β and λ, and kernel bandwidths $\sigma_\mathcal{W}$ and $\sigma_\mathcal{V}$). α was set to 100 as commented in Sec.2.3.

The tuning of these parameters will pre-condition the data to be registered. This means that the registration can favor or be nearly invariant to one or several of the components listed above. For example, a large value of α will mean that the spatial scale is largely dilated with respect to the other ones. This implies that registration in this direction is not favored (if the kernel bandwidths $\sigma_\mathcal{W}$ and $\sigma_\mathcal{V}$ are not modified): the baseline data at a given location cannot be matched with the follow-up data at another location, even if the signals at these two locations may be relatively close. Thus, this favors the estimation of changes along the magnitude and temporal dimensions, and not along the spatial one.

Choice of α. As mentioned before (Sec.2.1.3), correspondence between the anatomical locations along the myocardium can be assumed after the spatial normalization step. Hence, one can choose a value of α that is high in comparison with β and λ, so that priority is given to changes along the temporal and magnitude dimensions, in comparison with the spatial one. In our setting, we chose $\alpha = 100$ and values for β and λ in the range of $\alpha/100$. Up to a certain extent, this shares similar interests with the simplifications and a-priori made in the transformation model of Durrleman et al. (2013) commented in Sec.1.1.4.

Despite this setting, it should be noted that the pairs of 2D curves $\left\{\left(\varphi_r^{OFF}(\mathbf{x}_i,.), \varphi_r^{FU}(\mathbf{x}_i,.)\right)\right\}_{i\in[1,N_\mathbf{x}^{REF}]}$ are not matched independently. Indeed, the definition of currents for the triangulated surfaces in Eq.1 joins adjacent temporal instants and spatial locations, which means that 3D surfaces are still considered in the registration process.

Choice of β and λ. In order to fix a balance between the estimation of changes along the magni-

	Baseline	**Follow-up**	p**-value**
Age ($years$)	55[34/72]		.
Male gender	5(33%)		.
Heart rate (bpm)	67[58/72]	52[57/71]	NS
LV volume			
end-diastolic (mL)	44[35/49]	39[35/55]	NS
end-systolic (mL)	12[10/17]	12[10/16]	NS
ejection fraction (%)	71[67/73]	69[65/75]	NS
Wall thickness			
septum (mm)	20[18/27]	20[16/26]	0.028
lateral wall (mm)	12[11/13]	11[10/12]	0.016
LV mass (g)	247[203/363]	257[170/364]	NS
LVOT			
gradient ($mmHg$)	80[51/100]	30[5/66]	0.005
gradient reduction (%)	.	$-70[-91/-7]$	.

Table 1: Clinical characteristics of the studied subjects (N=15). NS: Non-significant statistical difference (p-value from Wilcoxon signed-rank test > 0.05).

tude and temporal dimensions, the two following distances are defined:

$$d_V(\mathbf{x},t) = \|\hat{\varphi}_r^{FU}(\mathbf{x},t) - \hat{\varphi}_r^{OFF}(\mathbf{x},t)\| \qquad (8)$$
$$d_T(\mathbf{x},t) = \left| t - \underset{u}{\operatorname{argmin}} \|\hat{\varphi}_r^{FU}(\mathbf{x},t) - \hat{\varphi}_r^{OFF}(\mathbf{x},u)\| \right|$$

The distance d_V quantifies the (vertical) distance along the magnitude axis between the baseline and follow-up data at the location $(\mathbf{x}, t)$. Complementarily, the distance d_T looks for the time u at which the follow-up data is the closest to the baseline data at time t. The value it returns corresponds to the (horizontal) distance along the temporal axis between the baseline data at the location $(\mathbf{x}, t)$ and the follow-up data.

In practice, their computation is performed on signals resampled at a 10 times finer temporal scale $\{t_j\}_{j\in[1,N_t^*]}$ (obtained by bicubic spline interpolation, Fig.5a). This avoids that the discretization of the original motion data introduces bias in the computation of d_V and d_T.

Rescaling of the magnitude and temporal scales is chosen so that the average values of d_V and d_T over the data match, namely:

$$\beta_{balanced} = \frac{\mu_V}{\mu_T} \quad \text{and} \quad \lambda_{balanced} = 1, \qquad (9)$$

where:

$$\mu_V = \frac{1}{N_t^* N_{\mathbf{x}}^{REF}} \sum_{i=1}^{N_{\mathbf{x}}^{REF}} \sum_{j=1}^{N_t^*} d_V(\mathbf{x}_i, t_j)$$
$$\mu_T = \frac{1}{N_t^* N_{\mathbf{x}}^{REF}} \sum_{i=1}^{N_{\mathbf{x}}^{REF}} \sum_{j=1}^{N_t^*} d_T(\mathbf{x}_i, t_j)$$

A similar balance would have been achieved by setting $\beta = 1$ and adjusting λ accordingly.

On our data, this adjustment was set for each subject independently from the others. It can be considered as a normalization of the magnitude and temporal scales prior to the matching process.

3. Experiments and results

3.1. Patient population

The study included 15 HOCM patients (55 ± 20 years, 5 male) undergoing biventricular pacing. The research complied with the Declaration of Helsinki and the study protocol was accepted by our local ethics committee. Written informed consent was obtained from all subjects.

These patients had significant LVOT obstruction (baseline LVOT gradient of 80[51/100] $mmHg$) and a mean LV ejection fraction of 71[67/73] %).

An echocardiographic examination was performed at baseline and after $14(11-15)$ months of biventricular pacing, using a transthoracic probe (M4S or M5S, GE Healthcare, Milwaukee, WI) in a commercially available system (Vivid 7 or 9, GE Healthcare). Machine settings (gain, time gain compensation, and compression) were adjusted for optimal visualization, including harmonic imaging. The temporal region of interest was manually set to one cardiac cycle with approximately 100 ms additional margin around it. Average frame rate and pixel size were of 45 ± 18 fps (heart rate: 64 ± 9 bpm) and 0.28 ± 0.06 mm^2, respectively.

Follow-up data corresponded to the optimal pacing (inter-ventricular delay VV) retained during the implementation of the pacing device.

The baseline and follow-up characteristics for these subjects are summarized in Tab.1. Data are

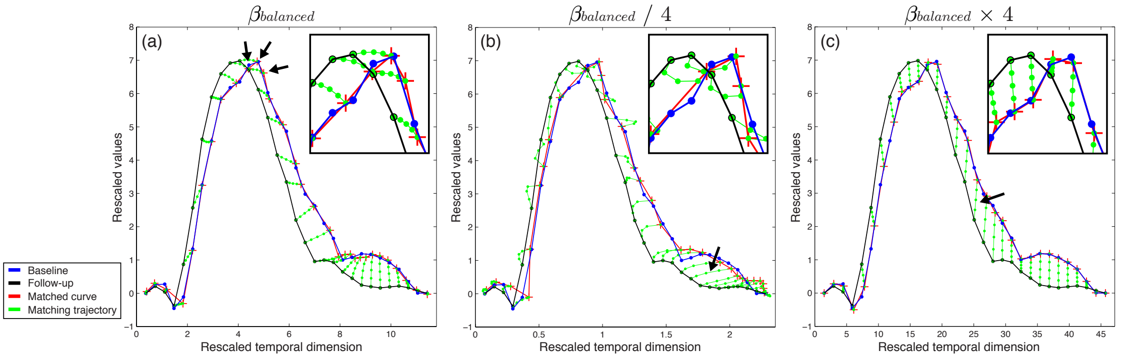

Figure 6: Influence of the rescaling factor β on the temporal dimension. Matching between the baseline (blue) and follow-up (black) data of Fig.5. The curved green trajectories correspond to the discretized geodesics followed throughout the steps of the diffeomorphic registration (Sec.2.2.2). The overall matching links the start- and end-points of the green curves, and is plotted in red. (a) balanced choice (Eq.9) between the magnitude and temporal dimensions. Adequate matching of the curve peaks and surrounding points is achieved (black arrows). (b) rescaling factor 4 times smaller: the matching along the temporal dimension is favored (notable changes indicated by the black arrow). (c) rescaling factor 4 times higher: the matching along the magnitude dimension is favored (black arrow).

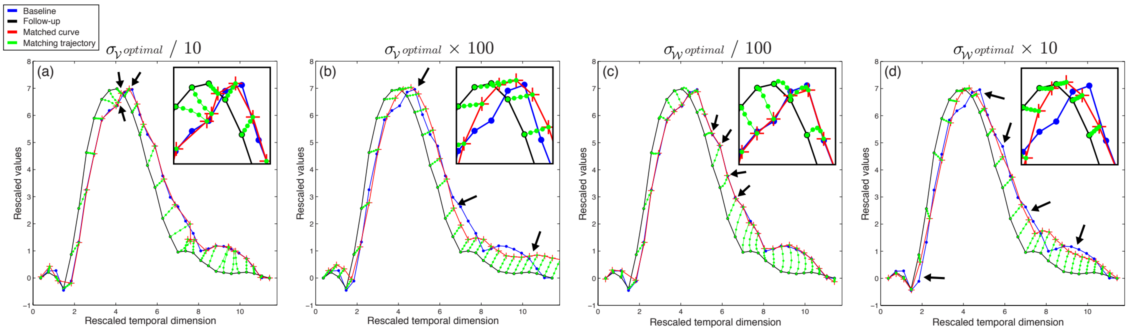

Figure 7: Influence of the kernel bandwidths $\sigma_{\mathcal{W}}$ and $\sigma_{\mathcal{V}}$, in comparison with the balanced choice mentioned in Sec.3.2.2 and shown in Fig.6. (a) $\sigma_{\mathcal{V}}$ 10 times smaller, resulting in inadequate matching of the curve peaks (black arrows): $\mathbf{v}_\tau$ is not smooth enough and does not constrain enough the geodesics direction at these locations, and therefore produces mismatch of the peaks. (b) $\sigma_{\mathcal{V}}$ 100 times higher, $\mathbf{v}_\tau$ is too smooth, which results in few variations in the geodesics direction and poor matching of the curves (black arrows). (c) $\sigma_{\mathcal{W}}$ 100 times smaller, resulting a too low smoothness of the currents, and therefore too many local deformation and poor tolerance to match landmarks out of other landmarks (black arrows). (d) $\sigma_{\mathcal{W}}$ 10 times larger, resulting in a too large smoothness of the currents, and therefore little local deformation and poor matching of the curves (black arrows).

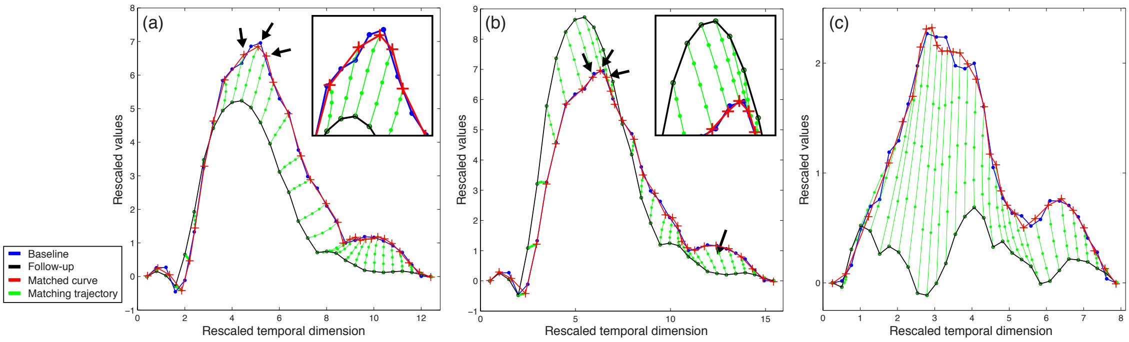

Figure 8: Quality of the registration output against different shape evolution configurations (accurate matching of the curve peaks is indicated by the black arrows). (a) and (b): follow-up data from Fig.5b rescaled by 0.75 and 1.25, respectively. (c) Completely different temporal trajectories obtained from the data at other locations.

Preprint version accepted to appear in Medical Image Analysis.
Final version of this paper available at http://www.sciencedirect.com/science/article/pii/S1361841514001510

presented as median and first/third interquartile range. A non-parametric statistical test (Wilcoxon signed-rank test) was used for the comparison of paired data (baseline vs. follow-up). The level of statistically significant differences between the tested groups was set to p-values below 0.05. Such tests were performed using the SPSS statistical package (v.15.0, SPSS Inc., Chicago, IL).

Patients were separated according to the relative reduction of LVOT pressure gradient between baseline and follow-up. Threshold was set to 50% (significant reduction). Reduction was significant for $N = 7$ patients, and non-significant for $N = 6$ ones. Gradient data was not accessible for 2 patients, which were processed but discarded from the observations using the response data.

3.2. Evaluation of the diffeomorphic registration via currents

The dataset in Fig.5b was used to evaluate the behavior of the registration algorithm under different sets of parameters and retain the ones to work with for our clinical application. It corresponds to the radial displacement data of a given subject at two neighboring locations, visible in the two 2D curves delineating the 3D shape in Fig.5b. For the sake of clarity, the visualization in Fig.6, 7 and 8 was limited to the plane of one of these two curves. Despite the fact these data lie in a 3D space, no information is hidden by this 2D view. Indeed, the spatial dimension was scaled by a large value of $\alpha = 100$ (Sec.2.3). Thus, the baseline data at one location cannot be matched with the follow-up data at another location, and the transformation of each 2D curve lies within its 2D plane.

3.2.1. Evaluation of the scaling parameters

This dataset led to a value of $\beta_{balanced} \approx 0.37$, with $\lambda_{balanced}$ arbitrarily kept at $\lambda = 1$.

The influence of changing this balance is illustrated in Fig.6. These tests featured the registration parameters justified in Sec.3.2.2.

It can be observed that a too low value for β would favor the estimation of changes only along the temporal dimension (Fig.6b). From a clinical point-of-view, despite our interest for the estimation of such changes, this type of behavior is not relevant at all. Data are mismatched (curve peaks) despite similar shape evolutions. In addition, the temporal changes at end-diastole are overestimated, as pointed out by the black arrow in Fig.6b. This is physiologically impossible: pacing affects the timing of the systolic period and subsequent early-diastole; it also has some influence on the effect of atrial contraction on the ventricular displacement curves (end-diastole), but this latter point is reflected on the displacement magnitude and not on its timing.

Similarly, a too high value for β would favor the estimation of changes only along the magnitude dimension, and would be almost equivalent to computing point-to-point differences between the two curves (Fig.6c).

These effects would be worsened in case of very different shape evolutions. In contrast, the balanced option can reach more meaningful results even in this type of situation (Fig.8c).

3.2.2. Evaluation of the registration parameters

In practice, the implementation of the registration method uses a discrete scheme to build the diffeomorphism. In other terms, τ does not vary continuously between 0 and 1, but is replaced by its discrete version $\{\tau_n = \frac{n}{N_{steps}}\}_{n\in[0,N_{steps}]}$. In our experiments, we used a number of discretization steps of $N_{steps} = 5$. Few changes were observed with higher values. This is probably because we are not completely in a “very large deformation” framework, as initially targeted in Glaunès (2005).

We also used a 5-levels multiscale implementation (Glaunès, 2005) to better balance between the matching of the overall shape and the matching of shape points (the instants and locations where we have data).

The kernel bandwidth $\sigma_{\mathcal{W}}$ was set to $\sqrt{\mu_V^2 + \mu_T^2}$, which is in the order of magnitude of the overall distance between the data to match. The kernel bandwidth $\sigma_{\mathcal{V}}$ was set to $2 \cdot \mu_T$. This value is higher than the observed distance between the curve peaks (when present), and therefore constrains enough the registration so that peaks are not mismatched (see zooms in Fig.6a [correct matching] and Fig.7a and b [bad matching due to $\sigma_{\mathcal{V}}$]). This condition is large enough so that this tuning can be transported to the other patients of our dataset. Experiments illustrating the influence of different bandwidth choices are shown in Fig.7.

Finally, the weighting between the regularization and similarity terms was set to $\gamma = 1$ to balance their contributions.

Complementary experiments test the robustness of the registration against different shape evolution

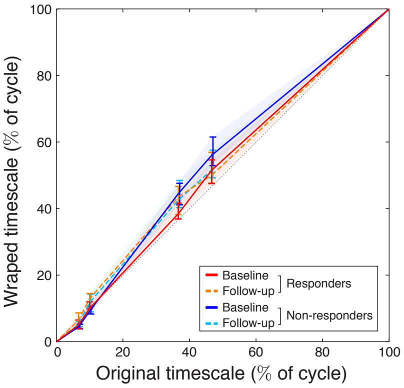

Figure 9: Variability in the temporal variations removed in the normalization steps, complementary of the values in Tab.2. Baseline and follow-up data, for the groups of responders and non-responders. The diagonal dashed line corresponds to no alignment (an event in the warped timescale is at the same position than in the original timescale).

(%)	Baseline	Follow-up	p-value
Responders			
MVC	5.0 [3.9 / 6.7]	6.5 [4.2 / 8.8]	NS
AVO	10.0 [9.8 / 12.1]	12.9 [8.3 / 14.6]	NS
AVC	38.5 [36.7 / 42.4]	43.6 [37.0 / 47.4]	NS
MVO	51.5 [46.7 / 54.9]	50.0 [46.9 / 57.9]	NS
Non-responders			
MVC	4.4 [3.6 / 5.4]	5.2 [4.5 / 6.3]	NS
AVO	9.2 [8.3 / 10.8]	11.7 [8.9 / 14.9]	0.028
AVC	44.5 [40.3 / 48.2]	42.6 [40.2 / 48.9]	NS
MVO	56.0 [52.9 / 61.6]	51.5 [49.2 / 58.5]	0.028

Table 2: Variability in the temporal variations (% of cycle) removed in the normalization steps, complementary of the curves in Fig.9. Differences between responders and non-responders were non-significant in all cases.

configurations of the input signals (Fig.8). Notably, accurate matching of the curve peaks is also reached in these configurations.

3.3. *Results on clinical data*

3.3.1. *Contribution of the normalization steps*

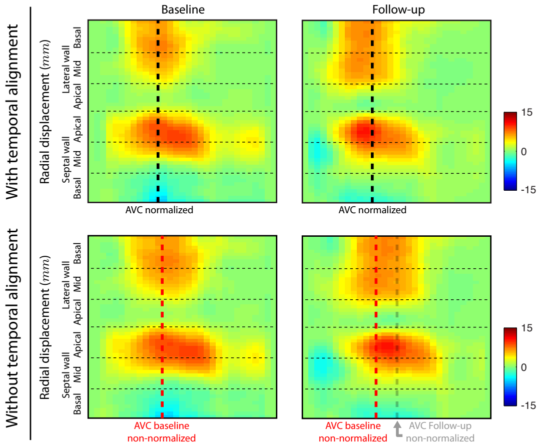

Figure 10: Myocardial displacement maps at baseline and follow-up for the patient shown in Fig.2, with and without temporal normalization. The instant corresponding to AVC is indicated in dashed line: after temporal normalization (top), and original position within the cycle without temporal normalization (bottom).

The method was tested on each of the patients described in Sec.3.1. The variability in the temporal variations removed in the temporal normalization steps is summarized in Fig.9 and Tab.2. No normalization means that an event in the warped timescale is at the same position as in the original timescale. This corresponds to the diagonal dashed line. Higher variability is observed for the end-systolic events (AVC and MVO). Slight differences were observed between the baseline and follow-up data for the AVO and MVO events in the non-responders group. However, differences between responders and non-responders were non-significant in all cases. This confirms that such physiological variations do not contain changes that might be correlated with the application of pacing, and therefore bias our analysis of the remaining changes between baseline and follow-up.

Nonetheless, maintaining the temporal normalization is crucial to prevent from bias in the analysis. Fig.10 illustrates the effect of the lack of temporal normalization on the displacement patterns observed for the subject of Fig.2. With temporal normalization, the lateral wall seems to activate earlier at follow-up, using the black dashed line corresponding to AVC as physiological marker. However, without temporal normalization, this activation would be considered as delayed at follow-up, using the red dashed line corresponding to baseline AVC as physiological marker. This comes from the fact that for this subject, instants for AVC are rather different between baseline and follow-up (39% vs. 50% of the non-normalized cardiac cycle, respectively). Complementary illustrations, showing that important characteristics of the patterns may be affected by the lack of temporal normalization, can be found in our earlier work (Duchateau et al., 2012b, 2014).

Finally, the initial spatiotemporal normalization (the limits defined by the physiological events) may

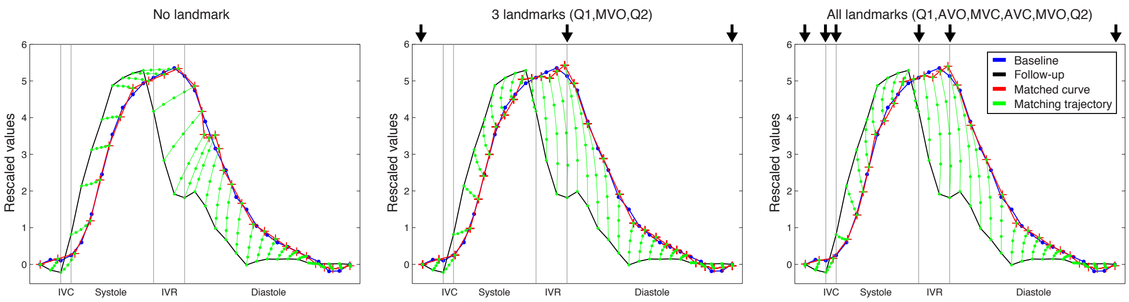

Figure 11: Quality of the registration output depending on the inclusion of a landmark-based similarity term (Sec.3.3.2) to enforce correspondence between specific physiological events (black arrows). Inadequate matching of the curve peaks is observed with the addition of this constraint.

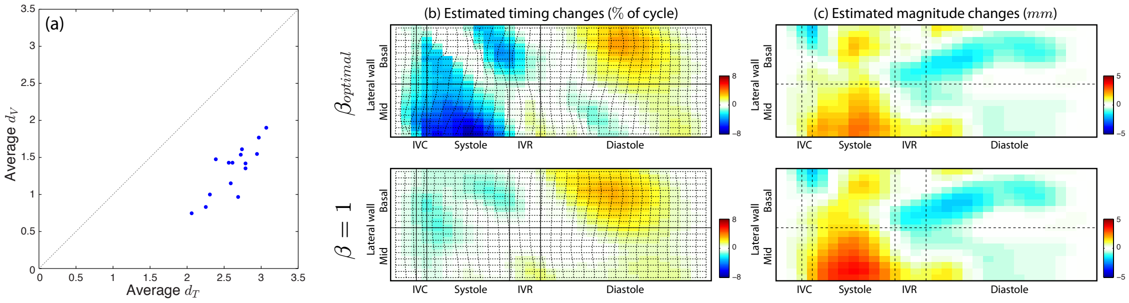

Figure 12: (a) Values of μ_V and μ_T determined for each subject at baseline and follow-up. (b) and (c) Comparison of the changes estimated by our method with $\beta_{balanced}$ and $\beta = 1$. Lateral wall of the patient introduced in Fig.2 (responder).

not be respected by the non-linear registration step. We actually tested the effect of constraining the registration using a landmarks-based similarity term in complement to the one already in use (Eq.6). This change is relatively straightforward in the implementation of Glaunès (2005); Vaillant and Glaunès (2005), as exemplified in Bogunovic et al. (2012). In our implementation, landmarks corresponded to physiological events of the cycle. This new term was weighted 1000 times higher than the previous one, to enforce correspondence between the desired physiological events. However, the corresponding results represented in Fig.11 indicate that the registration using this new constraint lacks flexibility to reach a clinically-plausible matching of the displacement curves. We therefore do not consider such additional spatiotemporal constraints for our specific application.

3.3.2. Generalizability of the scaling parameters

Figure 12a represents the values of μ_V and μ_T used to compute the scaling parameter $\beta_{balanced}$ (Eq.9), for each subject at baseline and follow-up. Low variability is observed among the whole set of subjects. The variability of $\beta_{balanced}$ is slightly higher. On our data, its 1st/2nd/3rd quartiles values were of 43.6, 52.5, and 58.2, while its min/max values were of 35.9 and 61.9. Thus, on these extremes cases, the balance between the magnitude and temporal dimensions may not be fully respected in case the median value 52.5 is used. As this may introduce bias in the analysis, we prefer to maintain the balance determined for each subject independently from the others, as commented in Sec.2.3.

Complementarily, Fig.12b and c compare the changes along the temporal and magnitude dimensions estimated by our method with $\beta_{balanced}$ and $\beta = 1$, on the lateral wall of the patient introduced in Fig.2 (responder). With the setting $\beta = 1$, changes along the magnitude dimension are overestimated and changes along the temporal dimension are under-estimated. In particular, the earlier activation of the lateral wall is almost not captured by this setting.

3.3.3. Computational issues

Septal and lateral wall data (basal and mid segments together) were processed independently due to computational time constraints. The 3D shapes were all made of 31 temporal instants, while the septal and lateral wall consisted of 18 spatial locations, resulting in 1020 different Dirac currents involved in the registration process. In contrast, the whole myocardial wall consisted of 53 spatial locations, resulting in 3120 different Dirac currents.

Processing the whole myocardial data of the patient shown in Fig.2 took 11.6 h, while average times for the septal and lateral walls were more than 7 times faster (1.6 $h \pm 10$ min and 1.5 $h \pm 14$ min, respectively, on a non-dedicated personal computer with 2.5 GHz Intel Core i5 processor and 4 Gb memory).

The use of the Improved Fast Gauss Transform (IFGT, Yang et al. (2005)), available as option in the implementation of Glaunès (2005); Vaillant and Glaunès (2005), avoids computing kernel convolutions and may substantially reduce the computational cost (up to 17 min for the whole myocardium, and around 110 s for the septal/lateral walls). However, inaccuracies in the computation may occur in the IFGT computation when our data is highly anisotropic (in our case, when $\alpha = 100$ with β and λ in the range of $\alpha/100$). We discuss these issues in App.B. Further improvements on this point may consider GPU implementations (Cury et al., 2013) or a matching pursuit on currents (Durrleman et al., 2009). However, we did not have access to such advanced implementations and used instead a publicly available one (Sec.2.2.2).

We checked that processing septal and lateral wall data separately had no influence on the results, provided this is done with the value of $\beta_{balanced}$ corresponding to the whole myocardial wall. Apart from the gain in computational time, a second reason justifying this processing and the discarding of apical data is that pacing-induced dyssynchrony mainly appears at the basal and mid levels (which moreover are the segments of interest for the LVOT obstruction).

3.3.4. Changes estimated by our method

Behavior along each dimension. There is no constraint to guarantee that the components of the transformation ϕ are diffeomorphic when looked at separately, contrary to what is settled in Durrleman et al. (2013). However, the transformations we manipulate are relatively small and/or smooth enough to prevent from these limitations. We checked this by computing the determinant of their Jacobian at each spatiotemporal location (full transform and each of its components), for each subject of our study. Values are summarized in Fig.13, which confirms the above suppositions. It represents the determinant of the Jacobian at each data point, for all subjects. All values are > 0 for the full 3D transform, the space-only and the time-only components. Notably, the Jacobian of the space-only component is almost 1, which confirms that the transformation of each point lies in the (time-magnitude) 2D plane. Values are also > 0 for the magnitude-only transform, except at two isolated locations in two different subjects (indicated by black arrows on the magnitude-only plot, for subjects #9 and #13). There, the determinant of the Jacobian for this component was -0.044 and -0.016, respectively. This may come from the fact that the spatial component of the transform is not completely the identity at these two locations, and to specificities of

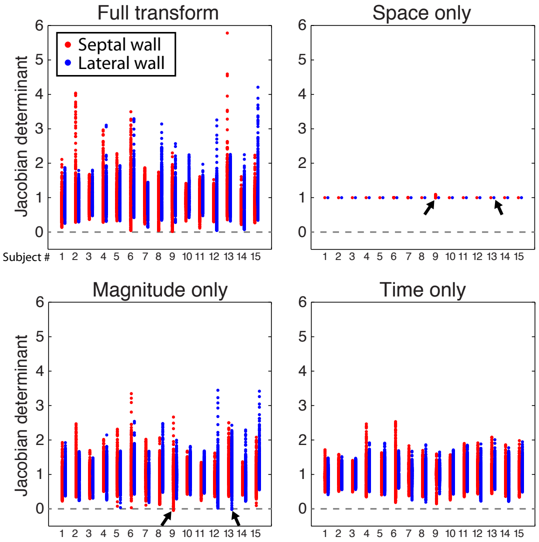

Figure 13: Determinant of the Jacobian at each data point, for all subjects. Full 3D transform (a), and space-, magnitude- and time-only components (b), (c) and (d). Black arrows on the magnitude-only plot indicate two isolated locations in two different subjects where the Jacobian of this component takes negative values (-0.044 and -0.016, respectively). Black arrows on the space-only plot indicate that the Jacobian of this component slightly differs from 1 at these locations.

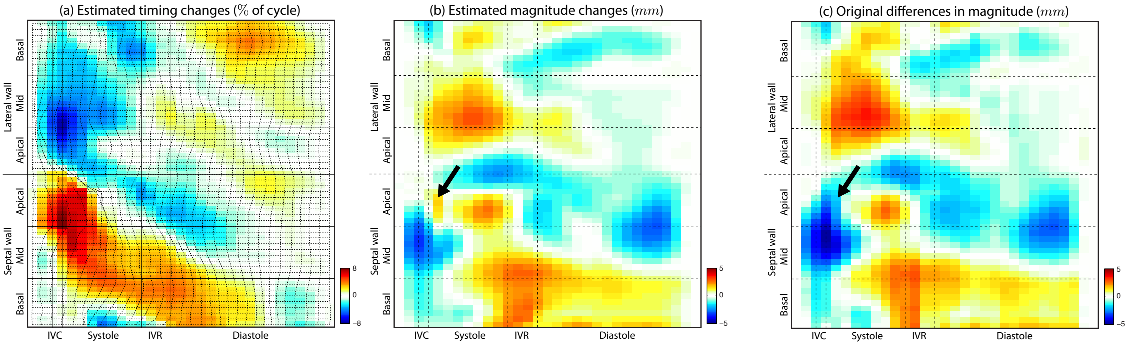

Figure 14: Changes estimated for the patient introduced in Fig.2 (responder). This patient showed significant reduction of the LVOT pressure gradient. (a) Changes along the temporal dimension estimated by our method. Both the earlier activation of the lateral wall (blue color) and the delay in the septal contraction (red color) are recovered. (b) Changes along the magnitude dimension estimated by our method. (c) Voxel-wise differences in magnitude between baseline and follow-up data, without using the registration part of our method. Black arrows point out physiological differences reflected by the local concavity/convexity of the represented maps, that taken into account by our method (Sec.3.3).

the shapes at these locations. This can be observed for one of these cases on the plot for the space-only component, where the Jacobian is not exactly 1 (black arrow on the space-only plot). In any case, these values are very low and isolated, and only affect the magnitude component, so that they do not bias our analysis. Specific care should be taken for a different application and a different parameter tuning.

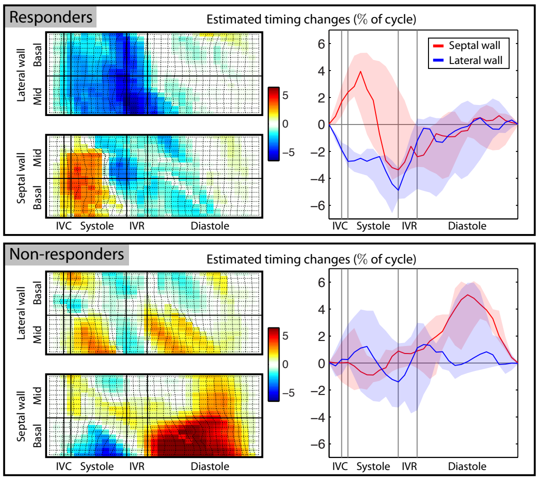

Figure 15: Changes along the temporal dimension estimated by our method for the subgroups of responders (top) and non-responders (bottom). Left: changes at each spatiotemporal location of the septal and lateral walls (median over the subgroup of patients). Right: spatial average of the changes over the septal and lateral walls, so that median and 1st/3rd quartiles over the subgroup of patients can be easily visualized. Earlier contraction of the lateral wall and delayed contraction of the septal wall are clearly observed for the whole subgroup of responders (low interquartile range). In contrast, this behavior is hardly observed for the non-responders.

Clinical findings. Figure 14a illustrates the changes along the temporal dimension estimated by our method for the patient introduced in Fig.2. Advance in the activation of the lateral wall is represented by blue color, and delay in the septal contraction by red color. Clinically, the LVOT obstruction for this patient was significantly reduced by pacing. The main changes in motion induced by pacing consist of the earlier activation of the lateral wall and the appearance of early-systole outward motion of the septum, as commented in Fig.2. The changes along the temporal dimension associated to these events are recovered by our method, as visible in Fig.14a.

Figure 14b illustrates the magnitude changes estimated by our method for this patient. The voxel-wise differences in magnitude between baseline and follow-up data are represented in Fig.14c for comparison purposes (original differences, without using the registration part of our method). These figures can be observed in parallel with the experiment of Fig.6a and c that showed close behaviors. Differences between the results of Fig.14b and c are visually subtle, but quantitatively meaningful. They reveal that we are not anymore estimating

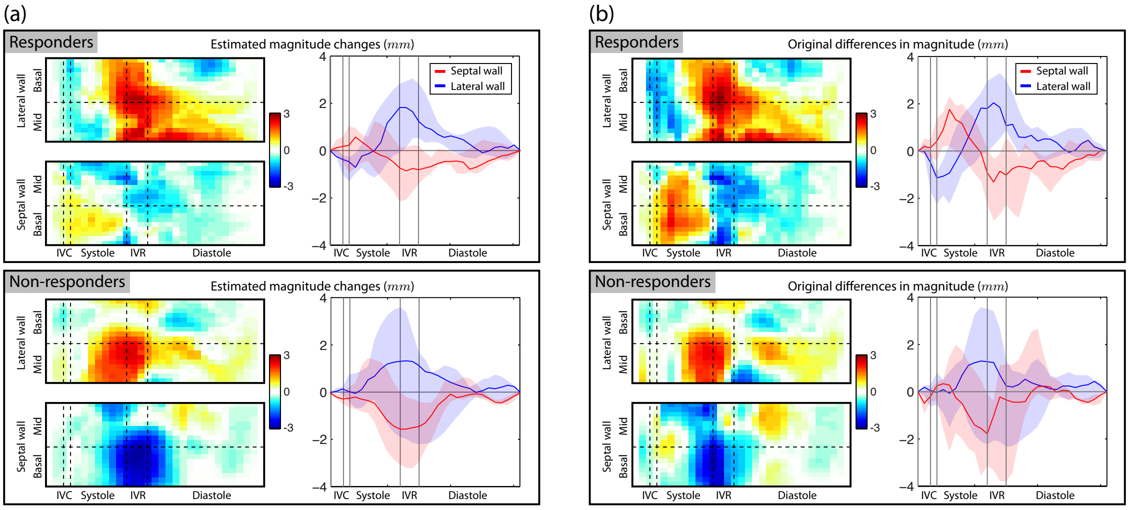

Figure 16: (a) Changes along the magnitude dimension estimated by our method for the subgroups of responders (top) and non-responders (bottom). (b) Voxel-wise differences in magnitude between baseline and follow-up data, without using the registration part of our method. Maps and curves were computed as in Fig.15. Responders and non-responders do not really differ in terms of patterns magnitude, while differences in terms of pattern timing were much clearer (Fig.15). Differences between the patterns depicted in the maps in (a) and (b) complement the observations of Fig.14b and c.

magnitude differences only, but a combination of changes along the temporal and magnitude dimensions (with balanced contributions, as set by our parameters). They first consist in a difference in the amplitude of the represented maps. Differences in the physiological behavior represented on the maps are also visible in the region of higher changes along the temporal dimension (mid and apical septum at early-systole, as pointed out by the black arrows). This information is of relevance for our application, as one of the clinically-relevant changes in motion appears in this temporal window on the septum.

Fig.15 represents information similar to Fig.14a, but for subgroups of patients separated according to the reduction in LVOT obstruction (Sec.3.1). Only temporal changes are represented, because of their direct relevance for our clinical application. They are shown as 2D spatiotemporal maps (median over the subgroup of patients, showing each spatiotemporal location of the septal and lateral walls) and 1D temporal curves (1st/3rd quartiles over the subgroup of patients, showing the spatial average of the estimated changes over the septal and lateral walls). The observations made for a single patient in Fig.14 (responder) are confirmed on the whole subgroup of responders (low interquartile range): the contraction of the lateral wall comes earlier and the contraction of the septal wall is delayed, probably as a consequence of induced early-systole outward motion. In contrast, this behavior is hardly observed for the non-responders (few changes globally observed over this subgroup and much larger interquartile range).

Fig.16 complements the information shown in Fig.15, by comparing the changes along the magnitude dimension estimated by our method with the voxel-wise differences in magnitude between baseline and follow-up data (without using the registration part of our method). This figure first shows that responders and non-responders do not really differ in terms of patterns magnitude, while differences in terms of pattern timing were much clearer (Fig.15). The changes in magnitude estimated by our method and the original differences in magnitude between baseline and follow-up data slightly differ in terms of values and concavity/convexity of the maps, which complements the observations of Fig.14b and c.

Finally, Fig.17 represents the changes along the temporal dimension estimated by our method (average over the considered wall during systole) against the pacing optimization used (the interventricular delay VV). Slight correlation is observed between the VV delay and the advance of the lateral wall contraction, further discussed in Sec.4. Observations for the subgroups of responders and non-responders are logically similar to the ones of Fig.15.

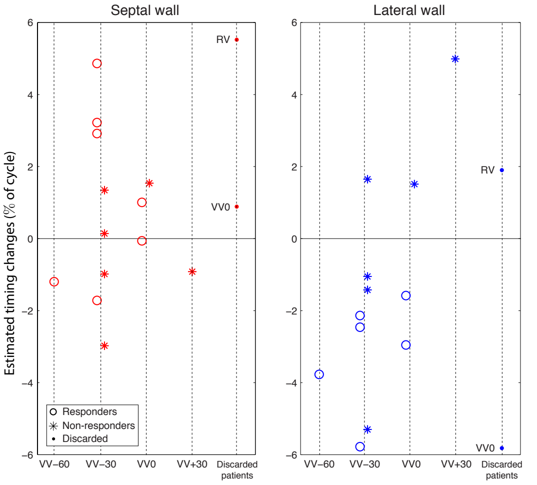

Figure 17: Changes along the temporal dimension estimated by our method for the whole set of patients (including the two patients not categorized as responders or non-responders). The horizontal axis stands for the pacing mode used (inter-ventricular delay VV). The vertical axis stands for the average of temporal changes over the septal/lateral wall during systole only (contraction phase).

4. Discussion

We have described a generic methodology to compare myocardial motion patterns in a quantitative manner. Our method consists of (i) the extraction and normalization of the features of interest (radial displacement, in our case), followed by (ii) diffeomorphic registration via currents in order to match baseline and follow-up data. Additionally, we provided insights into a generic way to adapt this registration scheme for tuning up the contributions of the spatial, temporal and magnitude dimensions to data changes, of interest for our application. Experiments include detailed testing of the parameters, and the statistical analysis of the data from 15 HOCM patients undergoing biventricular pacing to reduce LVOT obstruction.

We illustrated that our technique is of high interest for the assessment of pattern changes. More conventional measurements may be inappropriate (Sec.1.1.1). In contrast, our representation accounts for the motion patterns in their whole (at each spatial location along the myocardial wall and at each instant within the cycle). It enhances the visibility of specific features of interest, which are sometimes subtle to assess (e.g. outward septal motion at follow-up, slightly visible in Fig.2 and Fig.4, but highlighted by the warping estimated in Fig.14).

From a clinical point-of-view, we wanted to check that dyssynchrony was effectively induced as expected. Our method allows this assessment and proposes a quantitative analysis of such changes over the whole population. We remind that our original goal is not to discriminate between responders and non-responders. This is determined by the LVOT pressure gradient (non-invasive measurement), and already available in our protocol. However, we also demonstrated that our method can serve to study the link between the induced dyssynchrony and the gradient outcome. Responders and non-responders do not really differ in terms of patterns magnitude (Fig.16), but in terms of pattern timing (Fig.15). We confirmed that dyssynchrony has actually been induced as expected, and that gradient reduction most probably came from this. This finding complements the work in Giraldeau et al. (2013), which showed that the gradient reduction does not come from a deterioration of the cardiac function (local myocardial strain) despite the induced dyssynchrony. This clinical work was limited to the qualitative description of the pacing-induced pattern changes hypothesized by the clinicians. Our present work quantitatively confirms these pattern changes, and complements them by a statistical analysis that documents the behavior of subgroups of subjects. From a broader clinical perspective, this supports the clinicians' belief to continue in this therapeutical line, as initiated in Berruezo et al. (2011).

It should be noted that the estimation of such changes is made by a “blinded” algorithm. This means that no physiological a-priori is introduced to determine the “correct” matching between baseline and follow-up data. In fact, the notion of what is a “correct” matching is in itself discussable. In this philosophy, we opted for a neutral strategy with a balance between the similarity and regularization terms, and a balance between the magnitude and temporal components (Sec.3.2). This strategy highly depends on the application, but can also be taken from a generic point-of-view, which is why we discussed these balance notions. In any case, the relevance of the estimated values with respect to clinical expectations has also been discussed. The use of more physiologically-conditioned matching strategies is left for further clinical applications of our method.

Beyond the engineering problem of matching pairs of signals (myocardial motion maps), the registration strategy also defines a metric on the elements to be matched, which may be of interest. The warping of the source object to match the target one corresponds to the evolution along the geodesics defined by this metric. In the field of medical imaging, this has been investigated for morphometric analysis purposes, which involve statistics derived from this metric: e.g. principal geodesic analysis (Fletcher et al., 2004) or geodesic regression (Fletcher, 2013). Specific precautions can be taken for computing the average of the warping transformations (Arsigny et al., 2006). These were not considered in our study, when computing the average changes (Fig.15): in our case, the estimated transformations are relatively small, and the curvature of the geodesics is relatively low (Fig.6 and 8); additionally, the average is computed on one single component only (changes along the temporal or magnitude dimension).

Additional comments and limitations

We used $2\mathrm{D}+t$ echocardiographic sequences in a 4-chamber view, which are of relevance for our application. The analysis of $3\mathrm{D}+t$ data (Duchateau et al., 2013a) could improve our understanding of the pattern changes (myocardial displacement, velocity or strain naturally lie in a 3D space). However, the technique is not ready to be applied with a sufficient image quality and spatiotemporal resolution. Also, as mentioned in Sec.2.2, the adaptation of the pattern representation and registration to this type of data may be challenging.

As in a majority of clinical studies, patient behavior is discussed against the direct outcome of the procedure. In our case, the studied population was clustered according to the relative reduction of the LVOT pressure gradient. Naturally, the threshold retained for such a clustering conditions the interpretations. We set this threshold to a reduction $\geq 50\%$, based on our previous observations (Berruezo et al., 2011) and the available literature (Gersh et al., 2011; Vatasescu et al., 2012). However, the gradient value that is reached at follow-up may be another indicator of interest for response. Values lower than 30mmHg can be considered within the non-significant range, according to the guidelines (Gersh et al., 2011). On our dataset, both the relative gradient reduction and the gradient at follow-up indicators led to the same population clustering.

5. Conclusion

In this paper, we have built upon the recent advances in the statistical analysis of the functional information from cardiac images. We built a generic methodology for the estimation of local data changes, applied in our case to the quantification of changes in myocardial motion. Representing motion data as 3D shapes allows using state-of-the-art warping/registration techniques to match motion patterns, among which we chose one that is diffeomorphic and matches currents. Scalability of the data was introduced to tune up the contributions of the spatial, temporal and magnitude dimensions to data changes. We illustrated the method on the specific case of patients with hypertrophic obstructive cardiomyopathy ($N = 15$). We investigated the link between therapy-induced changes in myocardial motion patterns (pacing-induced dyssynchrony) and the clinical outcome (reduction of the left ventricular outflow tract pressure gradient). We discussed the interest of such a methodology to reach a more robust analysis of such complex patterns and subtle changes.

Appendix A. Repeatability of the motion extraction

The repeatability of the speckle-tracking procedure was evaluated by repeating the segmentation procedure and observing its influence on the radial displacement values, on one patient with medium quality images. The results for these experiments are summarized in Fig.18. Intra-observer variability (Fig.18b) was estimated from a single observer repeating the measurements 10 times. Inter-observer variability (Fig.18c) was obtained by comparing the measurements from 2 different observers. Finally, the variability inherent to the echocardiographic data (Fig.18d) was evaluated by comparing the measurements from 3 consecutive cycles of the same sequence and another cycle from a different sequence of the same patient (4-chamber view zoomed-in on the LV). Variability in the measurements is around 1.5mm. This is relatively low, considering that our application involves real data

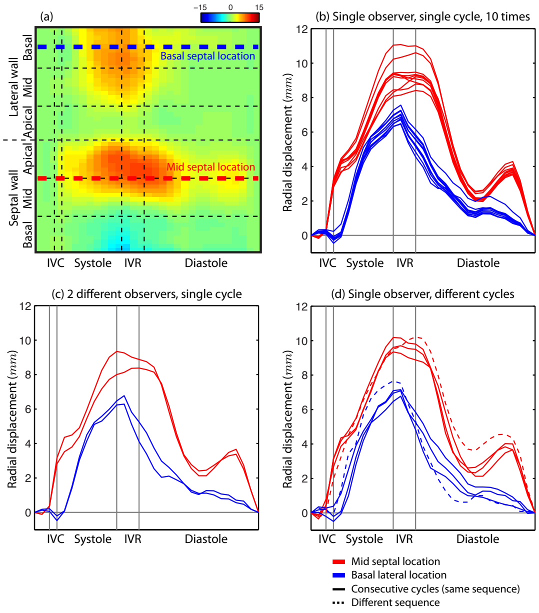

Figure 18: Repeatability in the extraction of myocardial motion, as conditioned by the speckle-tracking procedure. Traces shown for at the septal and lateral wall anatomical locations indicated over the top-left map (a), where clear contraction/relaxation patterns are observed. (b) Intra-observer variability (single observer, single cycle, repeated 10 times). (c) Inter-observer variability (2 different observers, single cycle). (d) Influence of the echocardiographic data (single observer, 3 consecutive cycles and 1 additional cycle from another sequence of the same patient [4-chamber view zoomed-in on the LV]).

from patients with abnormal cardiac shape (hypertrophic walls) and motion (under pacing at follow-up) with possibly low image quality. These data are therefore not straightforward to segment and track, including for experienced observers. The variability in our measurements also stands within the global accuracy ranges reported in the recent cardiac motion estimation challenges of De Craene et al. (2013) and Tobon-Gomez et al. (2013), which use simpler data (synthetic images, and plantom and volunteers data, respectively).

Appendix B. Computational issues related to the IFGT

We evaluated the accuracy of the IFGT (Yang et al., 2005) against the anisotropy introduced in our data through the factors α and β, keeping $\lambda = 1$. The implementation of Glaunès (2005); Vaillant and Glaunès (2005) allows to tune three of its parameters: the transform order, the cutoff ratio for targets, and the number of clusters (further details in Glaunès (2005)). It also provides a testing procedure, which is the one we used in this experiment. The first two parameters had lower influence on the IFGT accuracy, and default values were kept (5-th order and cutoff ratio of 9). In contrast, the number of clusters highly conditioned both accuracy and computational time, as summarized in Fig.19. To prevent from these errors and for the sake of generality, we decided not to use the IFGT computations in our final pipeline.

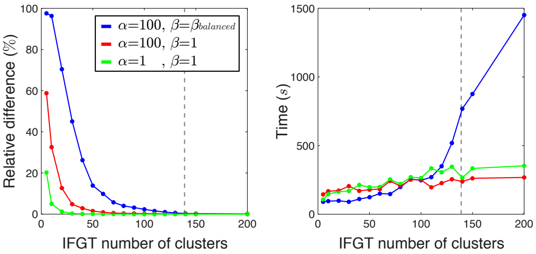

Figure 19: Accuracy and computational time for the IFGT upon different scaling considerations of our data. Tests on the lateral wall of the patient introduced in Fig.2.

Acknowledgments

The authors acknowledge the Spanish Industrial and Technological Development Center (cvRemod CEN-20091044), the Subprograma de Proyectos de Investigación en Salud, Instituto de Salud Carlos III, Spain (FIS-PI11/01709), the Comisión Nacional de Ciencia y Tecnología (FONDAP-15130011), and the European Union 7th Framework Programme (VP2HF FP7-2013-611823). GG was awarded the grant Bal Du Coeur from the Fondation de l'Institut de Cardiologie de Montréal. The authors thank Dr. G Piella for her careful review and Dr. C Butakoff for the discussions and bug fixing of the implementation of registration via currents.

Conflict of interest

None

References

Adam, D., Landesberg, A., Konyukhov, E., Lysyansky, P., Lichtenstein, O., Smirin, N., Friedman, Z., 2004. Ultrasonographic quantification of local cardiac dynamics by tracking real reflectors: algorithm development and experimental validation, in: Proc. IEEE Computers in Cardiology, pp. 337–40.

Aronszajn, N., 1950. Theory of reproducing kernels. Trans Am Math Soc 68, 337–404.

Arsigny, V., Commowick, O., Pennec, X., Ayache, N., 2006. A log-Euclidean framework for statistics on diffeomorphisms, in: Proc. Medical Image Computing and Computer Aided Intervention (MICCAI), LNCS, pp. 924–31.

Ashburner, J., Friston, K., 2003. Human Brain Function. 2nd ed.. RSJ Frackowiak, KJ Friston, C Frith, RJ Dolan, CJ Price, S Zeki, J Ashburner, WD Penny, eds. Academic Press. chapter Morphometry.

Ashburner, J., Hutton, C., Frackowiak, R., Johnsrude, I., Price, C., Friston, K., 1998. Identifying global anatomical differences: Deformation-based morphometry. Human Brain Mapping 6, 348–57.

Ashburner, J., Klöppel, S., 2011. Multivariate models of inter-subject anatomical variability. Neuroimage 56, 422–39.

Beg, M., Miller, M., Trouvé, A., Younes, L., 2005. Computing large deformation metric mappings via geodesic flows of diffeomorphisms. Int J Comput Vis 61, 139–57.

Behar, V., Adam, D., Lysyansky, P., Friedman, Z., 2004. The combined effect of nonlinear filtration and window size on the accuracy of tissue displacement estimation using detected echo signals. Ultrasonics 41, 743–53.

Berruezo, A., Vatasescu, R., Mont, L., Sitges, M., Perez, D., Papiashvili, G., Vidal, B., Francino, A., Fernandez-Armenta, J., Silva, E., Bijnens, B., Gonzalez-Juanatey, J., Brugada, J., 2011. Biventricular pacing in hypertrophic obstructive cardiomyopathy: a pilot study. Heart Rhythm 8, 221–7.

Bhatia, K., Rao, A., Price, A., Wolz, R., Hajnal, J., Rueckert, D., 2014. Hierarchical manifold learning for regional image analysis. IEEE Trans Med Imaging 33, 444–61.

Bijnens, B., Cikes, M., Butakoff, C., Sitges, M., Crispi, F., 2012. Myocardial motion and deformation: What does it tell us and how does it relate to function? Fetal Diagn Ther 32, 5–16.

Bijnens, B., Cikes, M., Claus, P., Sutherland, G., 2009. Velocity and deformation imaging for the assessment of myocardial dysfunction. Eur J Echocardiogr 10, 216–26.

Bogunovic, H., Pozo, J., Cardenes, R., Villa-Uriol, M., Blanc, R., Piotin, M., AF, F., 2012. Automated landmarking and geometric characterization of the carotid siphon. Med Image Anal 16, 889–903.

Charon, N., Trouvé, A., 2014. Functional currents: a new mathematical tool to model and analyse functional shapes. J Math Imaging Vis 48, 413:31.

Cikes, M., Sutherland, G., Anderson, L., Bijnens, B., 2010. The role of echocardiographic deformation imaging in hypertrophic myopathies. Nat Rev Cardiol 7, 384–96.

Cury, C., Glaunès, J., Colliot, O., 2013. Template estimation for large database: a diffeomorphic iterative centroid method using currents, in: Proc. Geometric Science of Information (GSI), LNCS, pp. 103–11.

De Craene, M., Marchesseau, S., Heyde, B., Gao, H., Alessandrini, M., Bernard, O., Piella, G., Porras, A., Tautz, L., Hennemuth, A., Prakosa, A., Liebgott, H., Somphone, O., Allain, P., Makram Ebeid, S., Delingette, H., Sermesant, M., D'hooge, J., Saloux, E., 2013. 3D strain assessment in ultrasound (Straus): a synthetic comparison of five tracking methodologies. IEEE Trans Med Imaging 32, 1632–46.

Duchateau, N., Bijnens, B., D'hooge, J., Sitges, M., 2013a. 3D echocardiography. 2nd ed.. T Shiota, ed. CRC Press. chapter Three-dimensional assessment of cardiac motion and deformation. pp. 201–13.

Duchateau, N., De Craene, M., Pennec, X., Merino, B., Sitges, M., Bijnens, B., 2012a. Which reorientation framework for the atlas-based comparison of motion from cardiac image sequences?, in: Proc. Spatio-Temporal Image Analysis for Longitudinal and Time-Series Image Data (STIA), MICCAI Workshop, LNCS, pp. 25–37.

Duchateau, N., De Craene, M., Piella, G., AF, F., 2012b. Constrained manifold learning for the characterization of pathological deviations from normality. Med Image Anal 16, 1532–49.

Duchateau, N., De Craene, M., Piella, G., Silva, E., Doltra, A., Sitges, M., Bijnens, B., Frangi, A., 2011. A spatiotemporal statistical atlas of motion for the quantification of abnormalities in myocardial tissue velocities. Med Image Anal 15, 316–28.

Duchateau, N., Doltra, A., Silva, E., De Craene, M., Piella, G., Castel, M., Mont, L., Brugada, J., Frangi, A., Sitges, M., 2012c. Atlas-based quantification of myocardial motion abnormalities: added-value for understanding the effect of cardiac resynchronization therapy. Ultrasound Med Biol 38, 2186–97.

Duchateau, N., Piella, G., Doltra, A., Mont, L., Bijnens, B., Sitges, M., M, D.C., 2013b. Manifold learning characterization of abnormal myocardial motion patterns: application to CRT-induced changes, in: Proc. International Conference on Functional Imaging and Modeling of the Heart (FIMH), LNCS, pp. 450–7.

Duchateau, N., Sitges, M., Doltra, A., Fernandez-Armenta, J., Solanes, N., Rigol, M., Gabrielli, L., Silva, E., Barceló, A., Berruezo, A., Mont, L., Brugada, J., Bijnens, B., 2014. Myocardial motion and deformation patterns in an experimental swine model of acute LBBB/CRT and chronic infarct. Int J Cardiovasc Imaging 30, 316–28.

Durrleman, S., Fillard, P., Pennec, X., Trouvé, A., Ayache, N., 2011. Registration, atlas estimation and variability analysis of white matter fiber bundles modeled as currents. Neuroimage 55, 1073–90.

Durrleman, S., Pennec, X., Trouvé, A., Ayache, N., 2009. Statistical models of sets of curves and surfaces based on currents. Med Image Anal 13, 793–808.

Durrleman, S., Pennec, X., Trouvé, A., Braga, J., Gerig, G., Ayache, N., 2013. Toward a comprehensive framework for the spatiotemporal statistical analysis of longitudinal shape data. Int J Comput Vis 103, 22–59.

Fletcher, P., 2013. Geodesic regression and the theory of least squares on Riemannian manifolds. Int J Comput Vis 105, 171–85.

Fletcher, P., Lu, C., Pizer, S., Joshi, S., 2004. Principal geodesic analysis for the study of nonlinear statistics of shape. IEEE Trans Med Imaging 23, 995–1005.

Fornwalt, B., 2011. The dyssynchrony in predicting response to cardiac resynchronization therapy: a call for change. J Am Soc Echocardiogr 24, 180–4.

Gersh, B., Maron, B., Bonow, R., Dearani, J., Fifer, M., Link, M., Naidu, S., Nishimura, R., Ommen, S., Rakowski, H., Seidman, C., Towbin, J., Udelson, J., Yancy, C., 2011. 2011 ACCF/AHA guideline for the diagnosis and treatment of hypertrophic cardiomyopathy: Executive summary: A report of the American College of Cardiology foundation / American Heart Association task force on practice guidelines. Circulation 124, 2761–96.

Giraldeau, G., Duchateau, N., Gabrielli, L., Penela, D., Evertz, R., Mont, L., Brugada, J., Berruezo, A., Bijnens, B., Sitges, M., 2013. Desynchronization effectively reduces left ventricular outflowtract obstruction without affecting systolic function in patients with hypertrophicobstructive cardiomyopathy, in: Eur Heart J-Card Img, EuroEcho abstracts, p. ii231.

Glaunès, J., 2005. Transport par difféomorphismes de points, de mesures et de courants pour la comparaison de formes et l'anatomie numérique. Ph.D. thesis. Université Paris 13.

Glaunès, J., Vaillant, M., Miller, M., 2004. Landmark matching via large deformation diffeomorphisms on the sphere. J Math Imaging Vis 20, 179–200.

Jasaityte, R., Heyde, B., D'hooge, J., 2013. Current state of three-dimensional myocardial strain estimation using echocardiography. J Am Soc Echocardiogr 26, 15–28.

Leitman, M., Lysyansky, P., Sidenko, S., Shir, V., Peleg, E., Binenbaum, M., Kaluski, E., Krakover, R., Vered, Z., 2004. Two-dimensional strain-a novel software for real-time quantitative echocardiographic assessment of myocardial function. J Am Soc Echocardiogr 17, 1021–9.

Lorenzi, M., Menze, B., Niethammer, M., Ayache, N., Pennec, X., 2013. Sparse scale-space decomposition of volume changes in deformations fields, in: Proc. Medical Image Computing and Computer Aided Intervention (MICCAI), LNCS, pp. 328–35.

Lorenzi, M., Pennec, X., 2013. Geodesics, parallel transport & one-parameter subgroups for diffeomorphic image registration. Int J Comput Vis 105, 111–27.

Maron, M., Olivotto, I., Betocchi, S., Casey, S., Lesser, J., Losi, M., Cecchi, F., Maron, B., 2003. Effect of left ventricular outflow tract obstruction on clinical outcome in hypertrophic cardiomyopathy. N Engl J Med 348, 295–303.

McLeod, K., Seiler, C., Sermesant, M., Pennec, X., 2013. Spatio-temporal dimension reduction of cardiac motion for group-wise analysis and statistical testing, in: Proc. Medical Image Computing and Computer Aided Intervention (MICCAI), LNCS, pp. 501–8.

Miller, M., Qiu, A., 2009. The emerging discipline of computational functional anatomy. Neuroimage 45, S16–39.

Miller, M., Trouvé, A., Younes, L., 2002. On the metrics and Euler-Larrange equations of computational anatomy. Annu Rev Biomed Eng 4, 375–405.

Nielsen, N., Carstensen, J., Smedsgaard, J., 1998. Aligning of single and multiple wavelength chromatographic profiles for chemometric data analysis using correlation optimized warping. J Chromatogr 805, 17–35.

Perperidis, D., Mohiaddin, R., Rueckert, D., 2005. Spatio-temporal free-form registration of cardiac mr image sequences. Med Image Anal 9, 441–56.

Qiu, A., Albert, M., Younes, L., Miller, M., 2009. Time sequence diffeomorphic metric mapping and parallel transport track time-dependent shape changes. Neuroimage 45, S51–60.

Russell, K., Eriksen, M., Aaberge, L., Wilhelmsen, N., Skulstad, H., Remme, E., Hauga, K., Opdahl, A., Fjeld, J., Gjesdal, O., Edvardsen, T., Smiseth, O., 2012. A novel clinical method for quantification of regional left ventricular pressure-strain loop area: a non-invasive index of myocardial work. Eur Heart J 33, 724–33.

Saitoh, S., 1988. Theory of Reproducing Kernels and its Applications. Pitman Research Notes in Mathematical Series, 189. Wiley.

Sakoe, H., Chiba, S., 1978. Dynamic programming algorithm optimization for spoken word recognition. IEEE Trans Acoust Speech Signal Process 26, 43–9.

Sakoe, H., Chiba, S., 2009. Canonical time warping for alignment of human behavior, in: Adv Neural Inf Process Syst, pp. 2286–94.

Tobon-Gomez, C., De Craene, M., McLeod, K., Tautz, L., Shi, W., Hennemuth, A., Prakosa, A., Wang, H., Carr-White, G., Kapetanakis, S., Lutz, A., Rasche, V., Schaeffter, T., Butakoff, C., Friman, O., Mansi, T., Sermesant, M., Zhuang, X., Ourselin, S., Peitgen, H., Pennec, X., Razavi, R., Rueckert, D., Frangi, A., Rhode, K., 2013. Benchmarking framework for myocardial tracking and deformation algorithms: an open access database. Med Image Anal 17, 632–48.

Trouvé, A., 1998. Diffeomorphisms groups and pattern matching in image analysis. Int J Comput Vis 28, 213–21.

Trouvé, A., Vialard, F., 2012. Shape splines and stochastic shape evolutions: A second order point of view. Quart Appl Math 70, 219–51.

Vaillant, M., Glaunès, J., 2005. Surface matching via currents, in: Inf Process Med Imaging, LNCS, pp. 381–92.

Vatasescu, R., Evertz, R., Mont, L., Sitges, M., Brugada, J., Berruezo, A., 2012. Biventricular / left ventricular pacing in hypertrophic obstructive cardiomyopathy: An overview. Indian Pacing Electrophysiol J 12, 114–23.

Vialard, F., Trouvé, A., 2010. A second-order model for time-dependent data interpolation: splines on shape spaces, in: Proc. Spatio-Temporal Image Analysis for Longitudinal and Time-Series Image Data (STIA), MICCAI Workshop, LNCS.

Yang, C., Duraiswami, R., Davis, L., 2005. Efficient kernel machines using the improved fast Gauss transform, in: Adv Neural Inf Process Syst, pp. 1561–8.

Zhou, F., De la Torre, F., 2012. Generalized time warping for multi-modal alignment of human motion, in: Comput Vis Pattern Recogn, pp. 1282–9.